This is a repository copy of *Colossal dielectric permittivity and superparaelectricity in phenyl pyrimidine based liquid crystals*.

White Rose Research Online URL for this paper:
https://eprints.whiterose.ac.uk/222043/

Version: Accepted Version

Article:

Panarin, Y.P., Jiang, W., Yadav, N. et al. (6 more authors) (2025) Colossal dielectric permittivity and superparaelectricity in phenyl pyrimidine based liquid crystals. Journal of Materials Chemistry C, 13 (3). pp. 1507-1518. ISSN 2050-7526

https://doi.org/10.1039/d4tc03561e

© 2025 The Authors. Except as otherwise noted, this author-accepted version of a journal article published in Journal of Materials Chemistry C is made available via the University of Sheffield Research Publications and Copyright Policy under the terms of the Creative Commons Attribution 4.0 International License (CC-BY 4.0), which permits unrestricted use, distribution and reproduction in any medium, provided the original work is properly cited. To view a copy of this licence, visit http://creativecommons.org/licenses/by/4.0/

Reuse

This article is distributed under the terms of the Creative Commons Attribution (CC BY) licence. This licence allows you to distribute, remix, tweak, and build upon the work, even commercially, as long as you credit the authors for the original work. More information and the full terms of the licence here: https://creativecommons.org/licenses/

Takedown

If you consider content in White Rose Research Online to be in breach of UK law, please notify us by emailing eprints@whiterose.ac.uk including the URL of the record and the reason for the withdrawal request.

eprints@whiterose.ac.uk
https://eprints.whiterose.ac.uk/

Colossal Dielectric Permittivity and Superparaelectricity in phenyl pyrimidine based liquid crystals

Yuri P. Panarin[1,2#], Wanhe Jiang[3#], Neelam Yadav[1#], Mudit Sahai[1,4], Yumin Tang[5],
Xiangbing Zeng[5], O. E. Panarina[1], Georg H. Mehl[3*], Jagdish K. Vij[1*]

[1]Department of Electronic and Electrical Engineering, Trinity College Dublin, The University of Dublin, Dublin 2, Ireland
[2]Department of Electrical and Electronic Engineering, TU Dublin, Dublin 7, Ireland
[3]Department of Chemistry, University of Hull, Hull HU6 7RX, UK
[4]Department of Physics, Birla Institute of Technology and Science, Pilani, India
[5]Department of Materials Science and Engineering, University of Sheffield, Sheffield, S1 3JD, UK

A set of polar rod-shaped liquid crystalline molecules with dipole moments (μ > 10.4-14.8 D), and molecular structures based on the ferroelectric nematic prototype DIO, are designed, synthesized, and investigated. When the penultimate fluoro-phenyl ring is replaced by phenylpyrimidine moiety, the molecular dipole moment increases from 9.4 D for DIO to 10.4 D for the new molecule and when the terminal fluoro- group is additionally replaced by the nitrile group, the dipole moment rises to 14.8 D. Such a replacement enhances not only the net dipole moment of the molecule, but it also reduces the steric hindrance to rotations of the moieties within the molecule. The superparaelectric nematic (N) and smectic A (SmA) phases of these compounds are found to exhibit colossal dielectric permittivity, obtained both from dielectric spectroscopy, and capacitance measurements using a simple capacitor divider circuit. The electric polarization is measured vs. the field (*E*). However, almost no hysteresis in *P* vs. *E* is found in the nematic and smectic A phases. The colossal dielectric permittivity persists over the entire fluidic range. The experimental results lead us to conclude that these materials belong to the class of superparaelectrics (SPE) rather than to ferroelectrics due to the absence of hysteresis and the linear dependence of *P* on *E*. The synthesized organic materials are the first fluids for which superparaelectricity is discovered and furthermore these show great potential for applications in supercapacitors used for storing energy.

==

joint first authors

*Corresponding authors: Y. Panarin: yuri.panarin@tudublin, G. Mehl: G.H.Mehl@hull.ac.uk; J. K. Vij: jvij@tcd.ie

Key words: Ferroelectric nematics, superparaelectric fluids, Colossal dielectric permittivity

1. Introduction

In electronics industries, the need for increasing the device density goes hand in hand with miniaturization of electronic structures that continue working efficiently with decreasing size to the nanoscale level. The micro and nano electronic devices thus require replacement of the conventional dielectric materials with those exhibiting colossal dielectric permittivity (CP). CP has been observed in solid state ferroelectric and superparaelectric (SPE) pervoskite related materials. The concept of superparaelectricity, introduced recently [1] is somewhat analogous to superparamagnetism (SPM). The electric polarization induced by the field is identified as superparaelectric with the basic property of the materials having CP. In an analogous case of magnetism, the theory of the ordered states based on isolated spins has been worked out. A superparamagnetic state includes small clusters of ordered spins with adequate magneto-crystalline anisotropic energy that maintain stability against thermal fluctuations. However, no theory is yet established for the solid SPE though polar clusters of varying sizes may exist to form a polar order.

These range mainly from the transition metal oxides [2,3] to two-dimensional nanosheet hybrids, the latter are based on reduced graphene oxide. [4] These systems are found having varying dependencies of the permittivity on temperature and frequency. For example, some SPE materials show CP independent of frequency up to the GHz range [5], while others such as the relaxor ferroelectrics show strong resonance-type frequency dependence of the permittivity [1]. In the paraelectric state, [1, 5] the solid state materials show softening of the permittivity with temperature increasing (soft mode), and in some cases the permittivity rises with increase in temperature. Due to these unusual properties for the new phenomenon, the paraelectric state is described as superparaelectric (SPE). The SPE materials have two common features (i) Colossal Permittivity CP [6] and (ii) the paraelectric type response (i.e. hysteresis-free linear P-E response).

The first examples of fluids that exhibit colossal dielectric permittivity are the recently observed ferroelectric nematics,[7, 8, 9,10] characterized by (i) extremely large dipole moments (μ ~10 D), (ii) colossal dielectric permittivity (ε′ ~ 10,000) and (iii) the high spontaneous polarization ($P_s \sim 5$ μC/cm^2) [11,12]. Such high dielectric permittivity was explained by two different theoretical models [13,14] and [15,16,17]. Interestingly, some materials show optical activity from mirror symmetry breaking [18,19,20] in both the ferroelectric and paraelectric nematic phases. Though several new organic ferroelectric compounds [21,22,23,24,25,26,27,28] continue being reported and discussed in the literature every week, many critical issues need addressing prior to fabricating and launching devices for applications. Though the structure property relationship of ferroelectric nematics has not yet been worked out, two major causes for the emergence of this phase have been found. These are (i) the magnitude of the molecular dipole moment and (ii) the relative spatial distribution of dipole moments of groups and or the charge distribution created within the molecule. Finally, the short and the long-range intermolecular interactions of the dipole moments of molecules lead to the mesoscale synergistic properties that need investigations.

In the quest for finding a novel class of high-dielectric constant organic materials based on the prototype molecule DIO [7], Table 1, the molecular design includes enhancing its dipole moment. Large molecular dipole moment is also the pre-requisite for obtaining large dielectric permittivity. In addition, the short-range Kirkwood Frohlich correlation parameter of the dipole moments [29] also plays an important role. In this paper, new molecules based on the substituted phenylpyrimidine motif are designed, synthesized, and investigated. Polarizing optical microscopy, X-ray scattering, electrical studies, and dielectric spectroscopy are used to characterize different phases of two new compounds. Large values of the dielectric permittivity imply dipolar orientation of the polar clusters at a microscopic level in the medium. Evidence for the existence of super paraelectricity in these materials is presented in terms of the absence of saturated polarization as a proof.

2. Experimental Section

2.1. Sample preparation for dielectric, optical and electro-optical studies.

For achieving planar alignment where required, Indium tin oxide (ITO) coated glass substrates are spin coated with RN 1175 (Nissan chemicals, Japan) and polymerized at a temperature of 250 ^{o}C for 1 hour. The coated surfaces are subsequently rubbed with a rotating commercial rubbing machine. While the homeotropic cells are coated with AL60702 (JSR Korea) and polymerized at 80 ^{o}C for 15 minutes and at 110 ^{o}C for 15 minutes respectively. Commercial cells procured from E.H.C ltd., Japan are also used for some of the measurements. The cell thickness was controlled by Mylar spacers of different thicknesses and it was measured by optical interference technique. LC cells of these samples are studied using polarizing optical microscope (Olympus BX 52) equipped with an INSTEC's hot stage. The temperature is controlled by Eurotherm 2604 and system designed to obtain temperature stabilization within ±0.02^{o}C

2.2. Differential Scanning Calorimetry

The DSC is investigated using Perkin Elmer Differential Scanning Calorimeter DSC 4000, using aluminum pans and calibrated against indium standard. DSC results are expressed in terms of the onset temperatures for second heating and the cooling curve. The heating rate, if not stated is 10 ˚C/min.

2.3. Birefringence Measurements

The birefringence measurements are made using an optical spectral technique [30] on a planar homogenous aligned 25 μm thick cell. The transmittance (T) spectrum of the cell from achromatic light source is measured using Avantes AvaSpec-2048 fiber spectrometer as a function of temperature. The transmittance T of a homogeneous planar aligned cell is given by:

$$T = A\sin^2\left(\frac{\pi\cdot\Delta n(\lambda)\cdot d}{\lambda}\right) + B \tag{9}$$

where A is the amplitude factor, B is leakage offset, d is the cell thickness and $\Delta n(\lambda) = k\cdot\frac{\lambda^2\cdot\lambda^{*2}}{\lambda^2-\lambda^{*2}}$ is the birefringence dispersion governed by the extended Cauchy equation.

Here k is a temperature-dependent scaling factor proportional to the order parameter (S). In contrast, λ^* is a temperature-independent dispersion parameter. The birefringence data for a wavelength of 550 nm are calculated using the software developed in the laboratory and the results obtained are plotted in Fig. 2.

2.4. X-ray diffraction

Simultaneously small and wide-angle X-ray Scattering (SAXS/WAXS) experiments were carried out at station I 22 of the Diamond Light Source. The samples are inserted in 1mm diameter glass capillary and is placed in a magnetic cell of field strength of ~0.5 Tesla in the horizontal direction placed on the top of a Linkam heating stage for temperature control. The X-ray wavelength used was 1.0 Å and 2D SAXS/WAXS patterns respectively were collected with two Pilatus detectors.

2.5. Dielectric Spectroscopy

Dielectric relaxation measurements over a frequency range 1 Hz–10 MHz were made using broadband Alpha High Resolution Dielectric Analyzer (Novocontrol GmbH, Germany). The glass substrates coated with a low sheet resistance (5 Ω/□) ITO electrodes were used to make cells. The reason for the low sheet resistance is that peak frequency arising from the sheet resistance of ITO in series with the capacitance of the cell is shifted to a frequency much higher than 1 MHz. A prior measurement of the capacitance of the empty cell is made. The measurement is carried out under the application of weak voltage 0.1V applied across the cell.

The temperature of the sample is stabilized to within ±0.05 °C. The dielectric spectra are analyzed using Novocontrol WINDETA program.

2.6. Electrical Measurements

An electric signal from Agilent 33120A signal generator amplified by high voltage amplifier (TReK PZD700) is applied across the cell. The output signal from the resistive (1 kΩ) or capacitive (2 μF) loads was monitored by a digital oscilloscope.

3. Results and Discussion

3.1. Molecular design of materials

This paper reports a study of the two newly synthesized phenylpyrimidines: WJ-16 and WJ-18 (Table 1). Here a fluorophenyl group of DIO is replaced by a narrower pyrimidine group and this replacement increases the molecular dipole moments from 9.4 D for DIO to 10.4 D for WJ-16.

Table. 1. The chemical structures of molecules WJ-16, WJ-18 and of the prototype DIO with the phase transition temperatures determined using polarizing microscopy. The dipole moments are calculated using DFT B3LYP/ 3-21G with the Gaussian View 9.0. Here N and SmA denote superparaelectric (SPE) nematic and smectic A phases.

Name of Compound	**Molecular structure**	**Phases and Transition Temperature (°C)**	**Dipole Moment (D)**
DIO	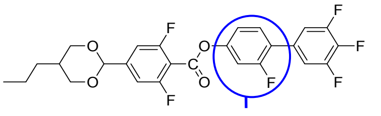	N_F 66.8 SmZ_A 83.5 N 173.8 I	9.4-9.5[7, 31]
WJ-16	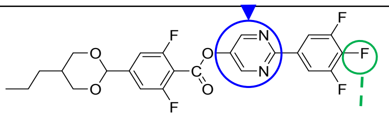	Cr 79.3 SmA 110.5 N 198.6 I	10.4
WJ-18	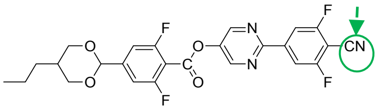	Cr 125.6 N 230 Decomposes	14.8

In WJ-18, the terminal fluoro-group is additionally replaced by the cyano-group. This increases its molecular dipole moment from 9.4 D for DIO to 14.8 D. It should be mentioned that this is not the highest dipole moment as compared to the giant dipole moment 33.5 D reported in the literature [22]. Details of the design, synthesis and chemical characterization of WJ-16 and

WJ-18 and their crucial intermediates are given in the supplementary Information (ESI, S1-S36; S41 gives DFT calculated structures). According to the ^{1}H-NMR spectroscopic data, WJ-16 does not contain isomers associated with the substitution pattern of the dioxane group, recently discussed for DIO. For WJ-18, small presence of the isomers is at the detection limit of ~1-2% (ESI, S13, S30). [32, 33] The dipole moments of the molecules are calculated using DFT Gaussian software suite at the B3LYP/ 3-21G (D, P) level. Use of the pyrimidine group instead of the fluorophenyl motif reduces the steric hindrance to the rotations of groups and it enables increased π-conjugation of the aromatic fragments, resulting in an increased planarity of the terminal aromatic rings. On cooling from the nematic phase WJ-16 additionally exhibits SmA phase. The transition temperatures are given in Table 1. In WJ-18, nematic above the crystal phase is observed, whereas the compound decomposes prior to reaching its N-Iso transition temperature. Differential scanning calorimetry (DSC) scanned at 10 ˚C min^{-1} on heating shows WJ-16 melting at 119.5 ˚C into the LC state, and it then transforming to the isotropic phase at 200.1 ˚C, with a transition enthalpy (ΔH) of 0.66 Jg^{-1} (0.21 kJmol^{-1}) (Figure S37, ESI). On cooling, a liquid crystalline phase emerges at 199.0 ˚C (ΔH: -0.67 J g^{-1}; -0.33 kJ mol^{-1}). A thermodynamically unstable (monotropic) additional LC phase emerges at 111.1 ˚C (ΔH: -0.22 J g^{-1}; -0.21 kJ/mol), prior to crystallization. WJ-18 shows the phase transition from the N to the crystalline state at 119.8 ˚C (Figure S38, ESI). Since the dipole moments of molecules are increased significantly as compared to DIO, dielectric permittivity for both WJ-16 and WJ-18 becomes colossal as discussed below.

3.2. The Optical Textures of Liquid crystalline phases.

For investigating the optical textures, we use commercial (E.H.C. Co. Ltd. Japan) and laboratory fabricated "uncoated" ITO electrodes cells of thicknesses varying from 2 to 25 μm, The planar/homeotropic alignment is achieved depending on the alignment layer put on to the cell electrodes. Fabrication of the cells in the laboratory involves spin-coating surfactant on the ITO surfaces of substrates. The handmade uncoated cells (i.e. without alignment layers, i.e. bare electrodes) are also used. Fig. 1 shows the textures obtained from polarizing optical microscopy (POM) of 9 μm cell filled with WJ-16 under different alignment configurations.

Textures of the planar aligned cells, where the rubbing direction (R) makes an angle of α = 45^o with the polarizer/analyzer (P/A) axis, are identical both in the nematic and the smectic phases except for a change in the color (Figure S39, ESI). This arises mainly from a large increase in the birefringence that occurs at the N-SmA transition temperature, under cooling. Some differences in the optical textures in the N and SmA phases are observed as the cell is rotated by a small angle, e.g. $\alpha \approx 5^o$, the rotation of the axis is indicated by a blue arrow drawn in Figure 1B. To explore it further, the POM textures of a planar aligned cell were recorded with the rubbing direction nearly parallel to the polarizer axis. Here, the observed texture in the N phase (Fig. 1A) highly fluctuates and is without domains – a typical feature of the conventional nematics. While the texture in SmA phase is non-fluctuating but has well defined domains (Figs. 1 B, C). These are the two typical features of smectics. It is worth noticing that textures of the parallel rubbed cells do not show 'twisted domains' - characteristionally found in ferroelectric [34,35] nematic phase (N_F) of DIO, but the texture appears domain-less rather like that of the ordinary nematics.

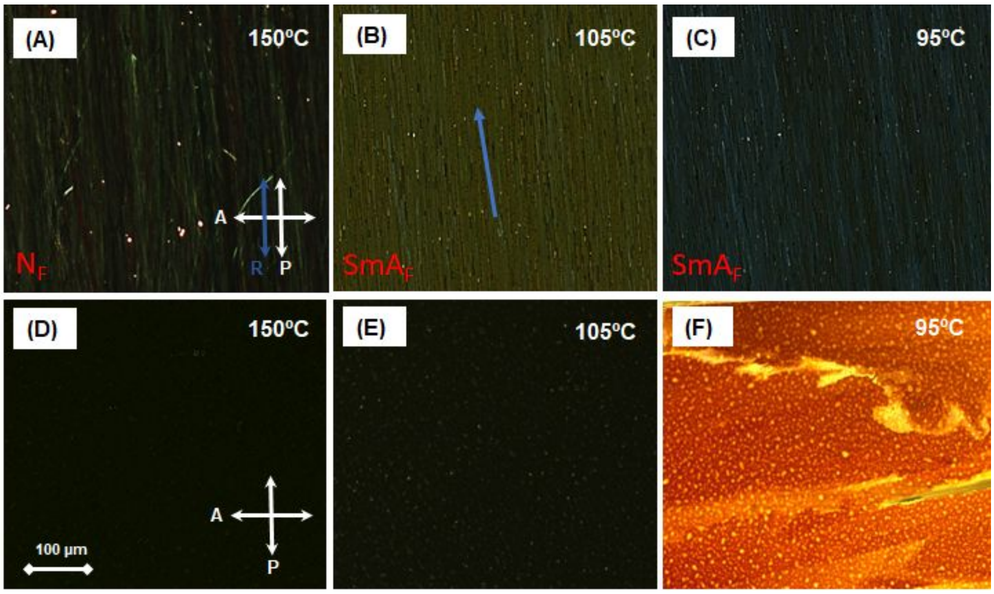

Figure 1. The POM textures of a homogeneously aligned planar cell **(A-C)** filled with **WJ-16** with the rubbing direction (in blue) lying parallel to the polarizer, and bare ITO cell using the same compound **(D-F)** at temperatures of 150 ˚C, 105 ˚C, and 95 ˚C. Here A and P refer to the analyzer and the polarizer, and R in blue refers to the rubbing direction in a planar aligned cell. The scale bar shown in 2D is of the length 100 µm.

Both WJ-16 and WJ-18 filled in commercial homeotropic cells show perfect homeotropic texture, in contrast to the texture of the N_F phase of DIO [7,1911] where the partial *Schlieren* texture is observed in a homeotropic aligned cell. WJ-16 when filled in uncoated cells (i.e.using bare ITO electrodes) shows perfect homeotropic texture with a large extinction in the nematic and SmA phases (Figures 1D, E). On further cooling the sample cell to a temperature of 95 ˚C, the texture transforms to that of a non-homogeneous planar cell (Figure 1F). This fortuitous property of obtaining homeotropic texture with bare electrodes allows us to record the dielectric spectra in homeotropic configuration without alignment layers. This is advantageous since the alignment layers may introduce uncertainty in the measurements of complex dielectric permittivity. WJ-18 displays only the nematic phase. However, in the uncoated cells, WJ-18 unlike WJ-16 does not show homeotropic alignment but gives non-homogenous planar texture (Fig. S40, ESI). We note that the isotropic phase of WJ-18 is unreachable due to its thermal decomposition occurring at a temperature of 230 ˚C.

To characterize the LC phases, the birefringence of WJ-16 is measured in a planar-aligned cell of 25 μm cell thickness and is calculated for a wavelength of 550 nm. Fig. 2 shows that the birefringence increases with decreasing temperature, and a significant step increase in birefringence occurs at the N to SmA transition temperature is observed. The behavior of these phases relates to the observed increase in the nematic order parameter *S*. This is verified by fitting the birefringence data to the empirical Haller equation [36] (shown as red line in Fig. 2) with $S_{\Delta T} = S_0(\Delta T)^{\gamma}$, where $\Delta T = T_{N\text{-}Iso} - T$, $\gamma = 0.25$. On using the wide-angle X rays scattering (WAXS) set-up where the sample alignment is achieved by external magnetic field, we obtain $\gamma = 0.28$ [Figure S42, Supplementary Information]. At the N to SmA phase transition temperature, the orientational order parameter increases significantly by as much as 0.16. This is a much larger step increase in the order parameter compared to the calamitic and bent-core LC systems reported in the literature. A comparison of the plots of the birefringence vs. temperature for WJ-16 with DIO shows that only a single nematic phase exists in WJ-16 unlike DIO, where more than one nematic phase is observed.

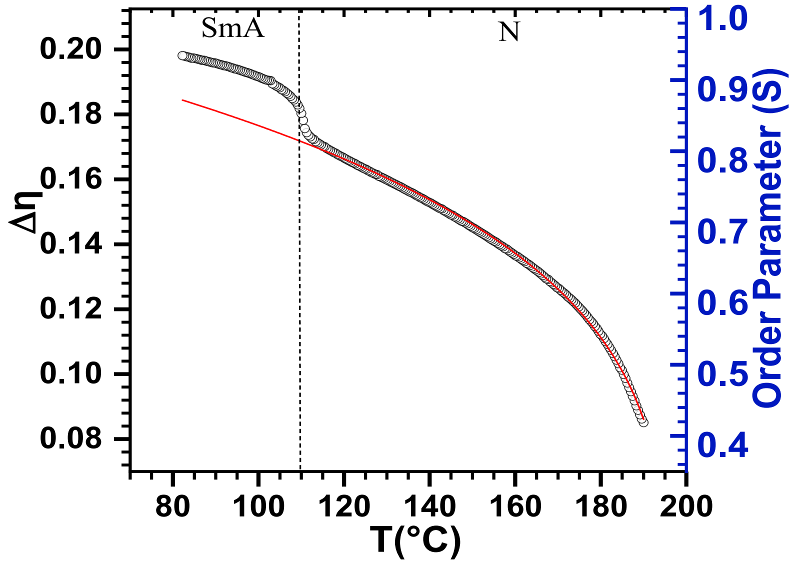

Figure 2. The birefringence (*Δn*) plot of **WJ-16** (with scale on the left Y-axis) and the order parameter (scale on the right Y-axis) as a function of temperature for a wavelength of λ = 550 nm obtained using a homogeneous planar aligned 25 μm thick cell. The red thin line is a fit of the Haller's equation to the birefringence data. Interestingly a significant increase in the order parameter (~0.16) occurs at the N to SmA transition temperature.

3.3. X-ray diffraction Study

To characterize the nanoscopic assembly behavior of WJ-16, small (SAXS) and wide angle (WAXS) X-ray scattering studies are carried out on magnetically aligned samples using synchrotron radiation. The nematic phase observed at temperatures between ~200 ˚C and 111 ˚C is characterized by a broad, but well oriented scattering peaks observed in both the small and the wide-angle regions (Figure 3A). The SAXS peak maxima lies in the horizontal direction, i.e., along the direction of the magnetic field. These observations indicate the average distance between the centers of molecules is 23.5 Å at 130 ˚C which is close to the molecular length found from molecular modelling (24 Å) and is consistent with the expectation that the molecular axes are oriented along the field direction. The main WAXS peak is observed in the vertical direction, with a corresponding *d*-spacing of ~4.5 Å. This again is consistent with the expected average distance between the molecules in the lateral direction. On cooling from the nematic phase, a sharp Bragg diffraction peak is observed at a temperature of ~111 °C, arising from a formation of the smectic phase. On further cooling, the sample goes to the crystalline state where multiple sharp Bragg peaks are seen in both SAXS/WAXS regions. The SAXS peak of the smectic phase has a corresponding *d*-spacing of 23.9 – 24.1 Å (q ~ 0.262 Å^{-1}). This again agrees with the molecular length, and it confirms that the phase is of SmA type, i.e., the average direction of the molecules is parallel to the smectic layer normal.

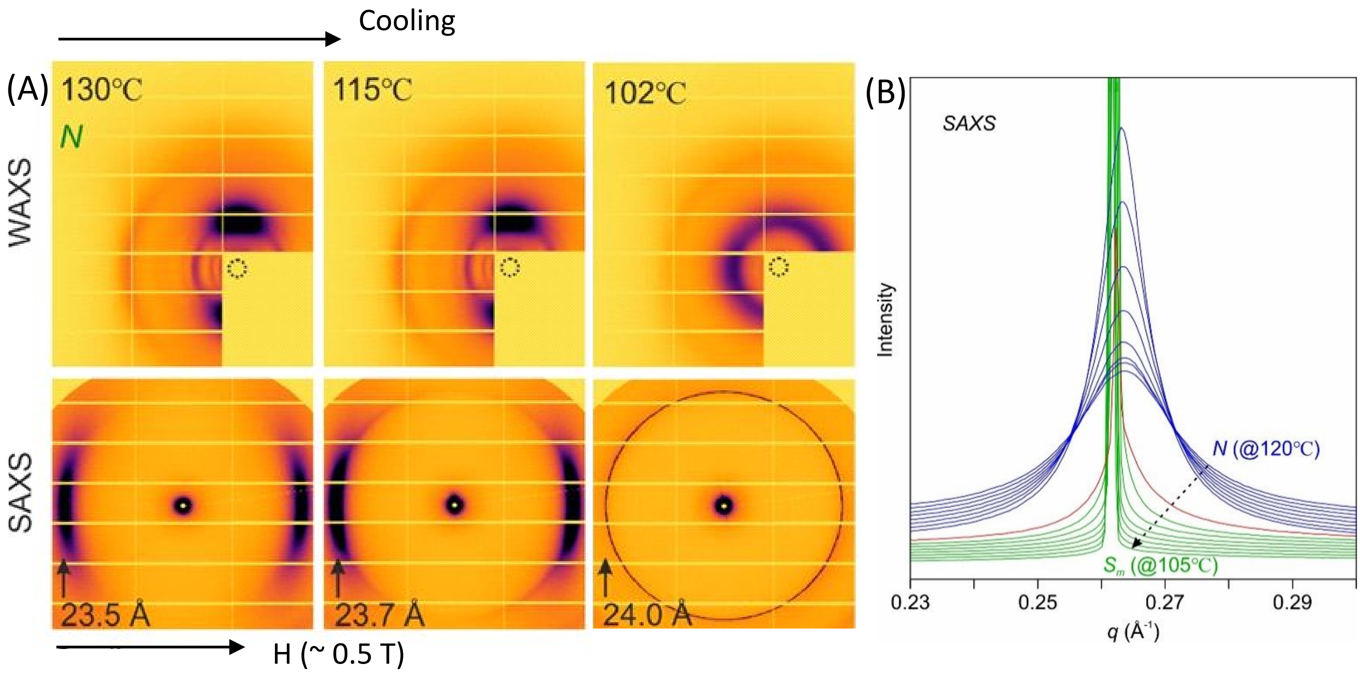

Figure 3. **(A)** Simultaneous SAXS/WAXS patterns of phases formed by **WJ-16** on cooling from 140 °C to 85 °C at a rate of 2 ˚C /min, with *d*-spacings of the scattering/diffraction peaks marked in SAXS. The WAXS beam center is indicated by a dashed circle, 3(**B)** 1D plot of

the SAXS intensities as a function of q for different temperatures (120 -105 ^{o}C), N is indicated in blue, SmA in green, the phase transition temperature N -SmA is shown in red.

The distinct sharpening of the small angle scattering peak with decreasing temperature at the transition from the N to SmA is shown in Figure 3B. The *d*-spacings observed in the N phase of WJ-16 are like those observed for DIO [7]. On the basis of the FWHMs of the SAXS and the WAXS peaks, we calculate the correlation lengths in the nematic phase both in longitudinal and lateral directions. The lateral correlation length is essentially constant in the entire N phase (~3.2 Å), thus confirming the liquid-like short range positional order of N-phase. However, the longitudinal correlation length decreases, first rapidly just above the SmA phase, from ~210 Å at 116 ˚C to ~100 Å at 122 ˚C, but then slowly to -50 Å at 150 ^{o}C and ~23 Å (single molecular length) just prior to the occurrence of the N-Iso transition (Figures. S43 and S44, ESI). The observed simultaneous SAXS/WAXS patterns of WJ-18 confirm formation of the N phase between the crystalline and the isotropic states. The SAXS peak has *d*-spacing of ~25.0 Å, almost the same as the length of WJ-18 molecule. The wide angle scattering in the vertical direction centers around 4.7 Å, suggesting a slightly larger side-way distance in the N phase. On heating the crystalline sample melts at ~180 ˚C, whereas on cooling it crystallizes at 130 ˚C at the rate of 2 ˚C/min. (Figures. S45 and S46, ESI)

3.4. Electrical study and discussion of the hysteresis in *P* vs. *E*

The main objective of the molecular design was to enhance its dipole moment and to increase the dielectric permittivity to understanding the structure-property relationships and its correlation to the ferroelectric nematic phase in the related material such as DIO. We examined ferroelectric behavior or its absence in WJ-16 and WJ-18 through studies of the hysteresis in the polarization *P* vs. *E*. A conventional method of measuring the polarization as a function of *E* is using the Sawyer-Tower circuit [37,38]. In this circuit, sample is connected in series with a capacitor of a known value thus forming the capacitor divider electrical circuit. To obtain whether hysteresis in *P* vs. *E* is present, output of the capacitor divider circuit is connected to the Y-input, whereas the applied triangular voltage is connected to X-input in the X-Y mode of the oscilloscope. Figures 4A and 4B show electrical responses of the sample to applied triangular wave voltage signal of 100 V_{pp}, (subscript 'pp' to V stands for the peak-to-peak voltage) using (A,C) the capacitive and (B,D) the resistive circuits (the latter circuit is shown in the inset of Fig. 4B).

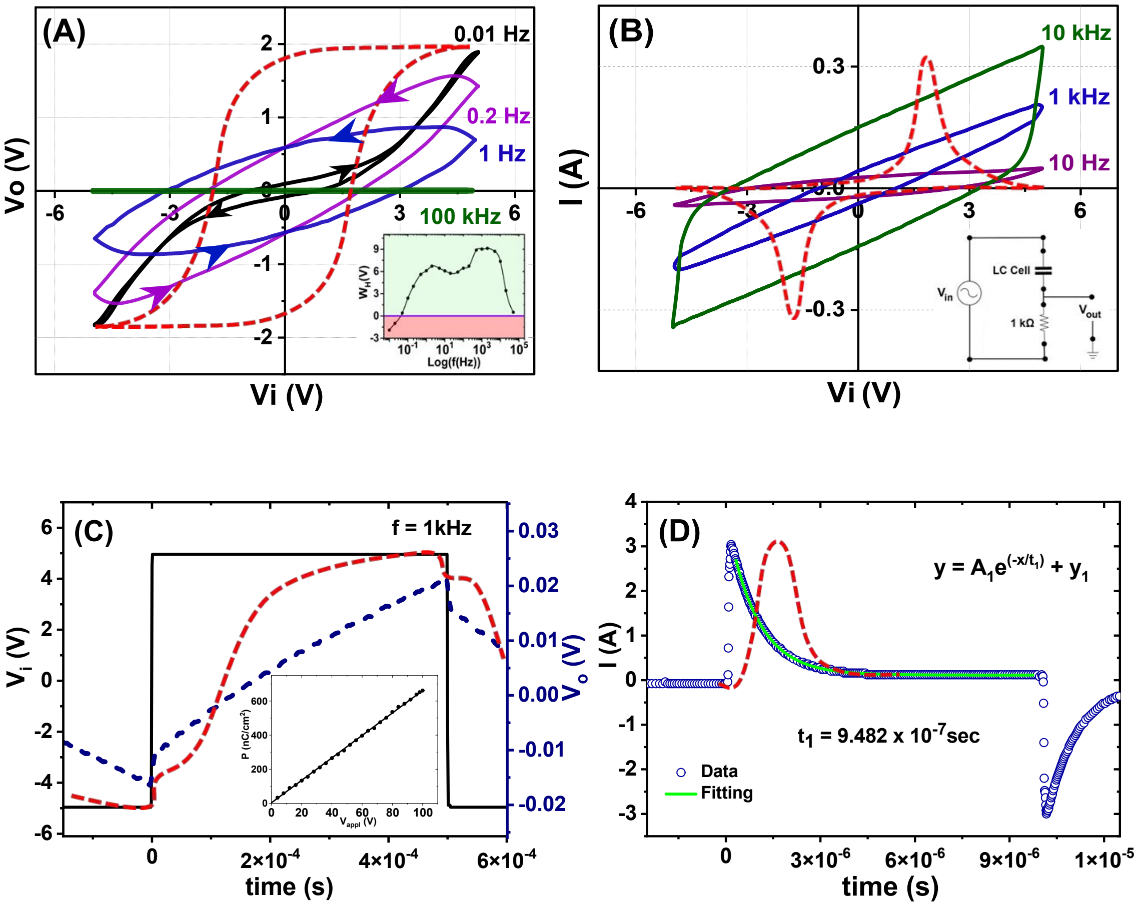

Figure 4. The capacitive **(A)** and the resistive **(B)** response of **WJ-16** filled 9 μm uncoated cell at 150 °C for different frequencies, 100 V_{pp} triangular voltage is applied (in the X-Y mode) of the oscilloscope. The inset in Figure 4A shows variation of the measured hysteresis width (W_H) as a function of frequency of the applied signal; **(C)** and **(D)** correspond to the recorded voltages across the capacitor (Vo) and the current (I) through the resistance on the application of 100 $V_{peak\ to\ peak}$ square voltage, connected to the oscilloscope in Y-t mode. Here, the red dashed lines correspond to anticipated ferroelectric hysteresis response, whereas the blue dash lines in C correspond to the actual voltage response and the blue data points in Fig 1 D represent the observed current response. Green line is a fit to the equation given in the inset of Fig. 4D.

Shape of the response curves can be considered "pseudo-hysteresis", i.e., the polarization lags behind electric field since the negative and the positive slopes do not match with each other. Furthermore, a saturation of P with E is not exhibited. The proof of the real classical hysteresis behavior is that saturation in the polarization P with E is observed, just like a dashed curve in Figure 4A. In our case, shape of the experimental response curve is far removed from the normal hysteresis curve (observed for DIO [7]). Shapes of such pseudo-hysteresis curves are strongly dependent on the frequency of the applied field, and these can easily be explained by the dynamic lag of the electric field [39]. It is to be noted that problem of finding the 'static hysteresis loop' experimentally is a challenging task and it was studied in detail in Ref. [40].

Firstly, the hysteresis loop width (the double coercive voltage) shows dynamic increase with frequency due to the dynamic delay in switching, [39] hence the frequency for a given applied field must be sufficiently low. Therefore, even with the absence in the saturated polarization, the dynamic curves can easily be denoted as the “pseudo-hysteresis” with hysteresis-like response. Secondly, the hysteresis width (or the double coercive force) continues to vary evenly in the low and ultra-low frequency ranges: from 1 Hz down to 10^{-4} [40] due to the screening effect arising from electronic charges due to the impurities that accumulate on the interface between the alignment layer and the dielectric medium. This effect explains the inverse (negative) hysteresis loop observed at very low frequencies of 0.01 and 0.2 Hz (Figure 4A). Hence we conclude no real ferroelectric hysteresis is observed in our samples. This is additionally confirmed by measuring the response using the resistive load (Figure 4B). Ferroelectric switching must lead to two distinctive peaks [41] as shown by dashed lines in Figure 4B. We do not observe these peaks for WJ-16 and WJ-18, thus proving that the switching behavior is not ferroelectric. In ferroelectric nematic phase of DIO, two current peaks are clearly visible in the N_F phase [7].

An alternative method of measuring the spontaneous polarization, using the circuit with the capacitive [42] and the resistive [9] loads, is to monitor the response across the load to the applied square-wave voltage in time domain (i.e., using the Y-t mode of the oscilloscope). This allows for simultaneous measurements of both the switching time and the rotational viscosity. Figures 4C and 4D show the observed voltage and the current responses using the capacitive (2 μF) and the resistive (1 kΩ) loads. Instead of the characteristic waveform obtained for ferroelectricity (shown by grey-dashed lines) in terms of the smooth voltage peaks arising from an integration of the re-polarization current [42], we observe classical paraelectric waveform. Similarly, for the resistive circuit, we expect the output to be Gaussian reported by Chen *et. al.* [9]. However, we observe only the exponential decay of the current but without the elongation of the pulse, a typical response from a conventional nematic LC.

Another way to check whether it is ferroelectric or not is to examine the dependence of *P* on *E*. The inset in Fig.4 shows the dependence of electrical displacement in 4 μm planar WJ-16 cell on applied sine-wave voltage. One may see that that this dependence is perfectly linear in both ways: on increasing and decreasing the applied amplitude voltage up to 100 V (25 V/μm) at which the induced polarization is ~0.7 μC/cm^2. We can estimate how far it is away from saturation. Assuming a typical (for such a large dipole moment) value of the spontaneous polarization ~5 μC/cm^2 [11,12], the expected saturation will occur at 500 V or higher. Hence, for the practical voltage applied, the P-E response is paraelectric-like.

The second harmonic generation (SHG) experiments are performed on these samples. Unlike ferroelectric nematic phases [7] the SHG signal was not observed, this confirmed the absence of ferroelectricity.

Summarizing, neither the hysteresis in P vs. E nor any other ferroelectric property was observed in the entire liquid crystalline temperature range of both WJ-16 and WJ-18.

3.5. Dielectric spectroscopy

In contrast to our expectations, both materials do not show presence of ferroelectricity in POM, P-E and SHG studies however they do show CP. To study the physical origin of this phenomenon we used the technique of dielectric spectroscopy, one of the most sensitive techniques for studying ferroelectric and other polar materials/phases. This was successfully employed for characterization of the ferro-[43,44,45,46] / antiferro- [47,48] and ferri-electric [49,50] liquid crystalline phases. Dielectric spectroscopy of WJ-16 and WJ-18 are investigated using Novocontrol high precision Impedance Alpha analyzer, employing initially commercial cells of different thicknesses with both homeotropic and planar alignments. The dielectric spectra were recorded in the frequency range of 0.1 Hz to 10 MHz with 0.1 V measuring AC voltage. The complex permittivity data were fitted to the Havriliak-Negami, eqn. (1) below, where the DC conductivity term is also included [51]:

$$\varepsilon^* = -\frac{i\sigma}{\varepsilon_0\omega} + \varepsilon_\infty + \sum_{j=0}^{n} \frac{\Delta\varepsilon_j}{\left[1+(i\omega\tau_j)^{\alpha_j}\right]^{\beta_j}} \quad (1).$$

Here ε^* is the complex permittivity and ε_∞ is the high frequency permittivity. The latter includes electronic and atomic polarizabilities of the material. ω is the angular frequency of the probe field, ε_o is the permittivity of free space, σ is the DC conductivity, τ_j is the relaxation time, $\Delta\varepsilon_j$ is the dielectric strength of the j^{th} relaxation process, α_j and β_j are the corresponding symmetric and the asymmetric broadening parameters of the distribution of relaxation times.

Initially the measurements were made using commercial cells with planar alignments. Figure 5D (Inset) shows temperature dependencies of the total dielectric permittivity (i.e. real part of complex permittivity, (ε') using 4 μm (blue filled triangle) and 9 μm (green filled diamond)) planar aligned cells. WJ-16 shows significantly large values of the dielectric strength (~200 and ~450) which could possibly be associated with ferroelectricity. However, it should be noted that the dielectric spectra of WJ-16 are different from the ferroelectric DIO material [52]. The dielectric permittivity WJ-16 is temperature independent in the entire temperature range, while the DIO shows temperature dependent soft-mode like behavior in non-ferroelectric phases (N, SmZ_A) and temperature independent permittivity in the ferroelectric nematic phase, N_F. The independence of the permittivity on temperature shown in Fig. 5D is rather ‘unusual behavior’ and this requires further investigation. Recently, the Boulder group (N. Clark et al.) found the effect of insulating alignment layers on the apparent/measured values of the dielectric permittivity [15]. In this case, the apparent capacitance C_{app} of LC cell can be expressed as two capacitances in series: the capacitance of the LC layer C_{LC} and capacitance of C_I of insulating alignment layer. Hence the apparent C_{app} $= \frac{C_{LC} \cdot C_I}{C_{LC}+C_I}$. There can be two possible opposite cases: the ordinary case where $C_{LC} \ll C_{I,}$ and the extraordinary case, where $C_{LC} \gg C_I$. In the ordinary one, i.e., in materials with the low/moderate dielectric permittivity, capacitance of the LC cell $C_{LC} \ll C_I$ and the apparent capacitance is the capacitance of LC cell, $C_{app} = C_{LC}$. Hence, in the ordinary case, this gives real value of capacitance and permittivity. However, in materials with very high dielectric permittivity ($\varepsilon >$ 10,000), such as the ferroelectric N_F phase and bent-core LCs [53,54] the capacitance of LC cell can easily exceed the capacitance of the alignment layer, $C_{LC} \gg C_{I.}$ In such a case, the apparent capacitance is limited by the capacitance of the insulating layers, C_I. We term it as the “Clark’s limit”, $C_{app} = C_I$. In our case however called extraordinary, the apparent $C(T)_{LC} \gg C_I$, the LC capacitance (and dielectric permittivity) would be limited by Clark’s limit C_I which is a constant over a reasonable range of temperatures.

Another important feature of the extraordinary case is that the apparent capacitance will be linearly dependent on the cell thickness [15]. Both features of the extraordinary case are supported by the results given in Fig. 5D. We can estimate the capacitance of the insulating alignment layers of our cells $C_I = \frac{\varepsilon_I \varepsilon_0 A}{2 d_I}$, and assuming the layer thickness d_I= 200 nm, and its permittivity as $\varepsilon_I \sim 5$, we obtain $C_I \sim 5.5$ nF. This capacitance limits the apparent value of the dielectric permittivity for the 4 μm cell to 100, in good agreement with the experimental value of 180, considering that the assumed values of thickness and permittivity of the alignment layer may be different from the actual values. To avoid this limitation and to get the actual values of the dielectric permittivity, one needs to increase the capacitance of the alignment layers C_I in approaching the ordinary case $C_I \gg C_{LC}$. The only way to achieve this is to reduce their thicknesses or simply use the uncoated metal/ITO electrodes as already used in some works reported in the literature [11,13,14,16,27, 55] and this allows us to measure the permittivity up to 50,000.

Following this approach, we performed the dielectric measurements of both WJ-16 and WJ-18 using handmade 4 μm cells with bare ITO electrodes. Figures 5 (A) and 5(B) show a three-dimensional (3D) plot of the real and imaginary parts of dielectric permittivity of 4 μm WJ-16 uncoated cell. Figure 1(C) shows the dielectric loss spectra for uncoated 4 μm WJ-16 cell taken at temperatures of 130, 180 and 200 °C with the corresponding fitting at 130 °C and (D). The temperature dependence of the total dielectric permittivity of the uncoated 4 μm cells WJ-16 and WJ-18.

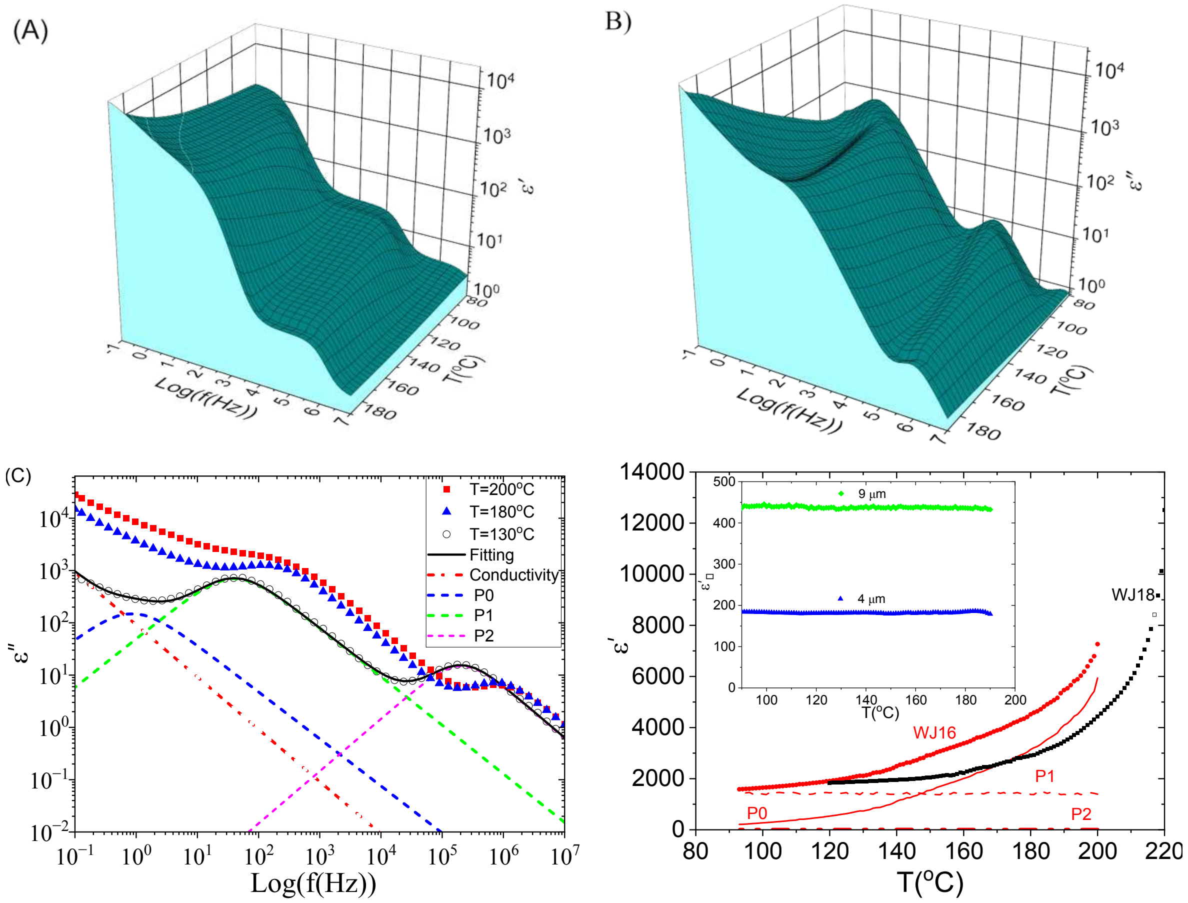

Figure 5 **(A) and (B)** show three-dimensional (3D) plot of the real and imaginary parts of dielectric permittivity of WJ-16 4 μm cell with bare ITO electrodes; **(C)** shows the frequency dependence of the imaginary part of permittivity at a temperature of 111 °C; circle symbols, ○, denote the experimental data, the solid black line is a fit to Eq. 1, while the blue, green and magenta dashed lines denote P0 (the electrode polarization process), relaxation processes P1 and P2, while the red dashed straight line with a slope of -1 represents the DC conductivity; **(D)** Temperature dependence dielectric permittivity for two 4 μm uncoated cells for WJ-18 (■) and WJ-16 (●) and dielectric strengths of three individual relaxation processes P0 (solid red line), P1 (dashed red) and P2 (dot-dash). **Inset**: Temperature dependence dielectric permittivity of two WJ-16 planar 4 μm (▲) and 9 μm (◊) cells

A comparison of the temperature dependencies of the total dielectric permittivity of 4 μm planar aligned cell (Fig. 5D) and uncoated 4 μm cells (Fig. 5D) of WJ-16 shows that the dielectric strength of uncoated cell is about one order higher than of the planar aligned cell and it becomes temperature dependent. These two features reflect that the Clark's limit is avoided in the bare electrodes cell and the measured values should reflect the real value of the dielectric permittivity. One may note that in uncoated cells the dielectric permittivity is increasing with temperature and reaches maximal values in the isotropic phase. To understand this unusual feature, we focus on the individual relaxation processes which contribute to the total dielectric permittivity.

Figure 5C is an example of the fitting of the dielectric loss spectra to three relaxation processes at 130 °C. These are named as P0, P1 and P2 with increase in the relaxation frequency. During the fitting of the spectra to Eqn. (1) both stretching parameters (α, β) were initially not fixed for all processes. On fitting we obtain α=1 and β=1 for both P1 and P2. The stretching parameters values of unity imply that the relaxation processes are pure Debye. Normally in the conventional calamitic liquid crystals, there exist two individual relaxation processes, one around the short axis often called the 'flip flop mode' (observed at lower frequencies) and the second rotation around the long molecular axis (exhibited at higher frequencies). Since the dielectric strength of P1 is found to be much higher in homeotropic (not discussed in the present manuscript) than in planar-aligned cell, process P1 can be assigned to flip-flop mode and P2 correspond to the rotations around the long molecular axis, as reported in the literature [20,52,[56]]. The stretching parameter, α_0, for P0 lies in the range 0.65 - 0.9 depending on the temperature. Here P0 is assigned to the parasitic ionic relaxation dynamics, caused by the separation of positive and negative charges, their motions in opposite directions end by their accumulation on the two electrodes. The process P0 in the dielectric loss spectra is broadened and hence $\alpha < 1$. In other words, P0 is assigned to the space charge/interfacial polarization produced by the mobility of ions and finally to their accumulation on the electrodes.

Now we can explain the huge dielectric permittivity in the isotropic phase. Fig. 5(D) shows the temperature dependencies of the total dielectric permittivity using 4 μm uncoated cells for WJ-16 (red filled circle) and WJ-18 (black filled square) and the dielectric strength of processes P0 (solid red line), P1 (dashed red line) for WJ-16 which contribute mostly to the total dielectric permittivity. The parasitic ionic process P0 is strongly temperature dependent, while P1 is almost independent of temperature. At lower temperatures $\Delta\varepsilon 1 >> \Delta\varepsilon 0$ and the total dielectric permittivity is also almost temperature independent. However, the dielectric strength $\Delta\varepsilon_0$ of P0 grows quickly with temperature and at ~152 °C it exceeds the dielectric strength $\Delta\varepsilon_1$ and contributes mostly to the total permittivity. Therefore, the huge dielectric permittivity in high temperature range, including the isotropic phase is obviously due to the parasitic ionic process. A similar observation and explanation of the CP in isotropic phase was given by [57,58]

Now by ignoring the parasitic ionic process P0 let us examine the relaxation process P1 in greater detail. Most striking feature of this process is a CP (~1,500) which is independent of temperature and phase but linearly depends on the cell thickness, i.e dielectric strengths in 4, 9, 22 μm cell are 1500, 3000, 7000 correspondingly. The magnitude of dielectric strength of P1 is two-three orders of magnitude higher than in paraelectrics and about one order smaller than the Goldstone mode in ferroelectric nematics [7,8,26,27,31,56] and some bent-core LCs [53,54]. In these ferroelectric materials the dielectric strength strongly depends on bias voltage which suppresses the Goldstone mode [13,15,54,]. However our samples unlike ferroelectric materials show paraelectric-like, hysteresis free linear P-E response and this property together with the CP can be assigned to SPE which appears in the temperature range of the paraelectric and ferroelectric phases [59] In contrast to ferroelectric nematics the dielectric spectra of our materials do not depend on bias voltage due to the absence of the spontaneous polarization.

High dielectric permittivity very likely reflects extremely strong collective molecular dipolar contribution. In the solid state, SPE arises from well-aligned molecular clusters which also exist in bent-core LCs [53,54]. However, in our materials such clusters were not observed and the CP can be explained by response of the correlated conglomerates of molecules. The possible physical mechanisms will be discussed later.

Since results of the permittivity measurements by dielectric spectroscopy are currently hotly debated [14,15,17], to validate the obtained permittivity values, we use the direct capacitance measurements to support observation of the colossal permittivity CP.

3.6. Direct capacitance measurements.

The colossal dielectric permittivity (CP) obtained by dielectric spectroscopy of uncoated cells can be confirmed by direct capacitance measurements of the LC sample. By definition, dielectric permittivity, ε' is a ratio of capacitances of the filled and empty cell, so the direct capacitance measurements will give most reliable value for capacitance and permittivity irrespective of any physical model. We used a capacitor divider circuit, shown in the inset of Figure 7, the capacitive load, $C_0 = 2$ μF. The capacitance of LC sample is measured as $C_{LC} = C_0 \frac{V_0}{V_{in} - V_0}$, the real part of the permittivity is deduced from $\varepsilon'_{LC} = \frac{d \cdot C_{LC}}{\varepsilon_0 A}$. Figures 7A and 7B show frequency dependencies of the dielectric permittivity for different temperatures (SmA, N and the Iso phases) using 4 μm uncoated cells of WJ-16 and WJ-18, respectively.

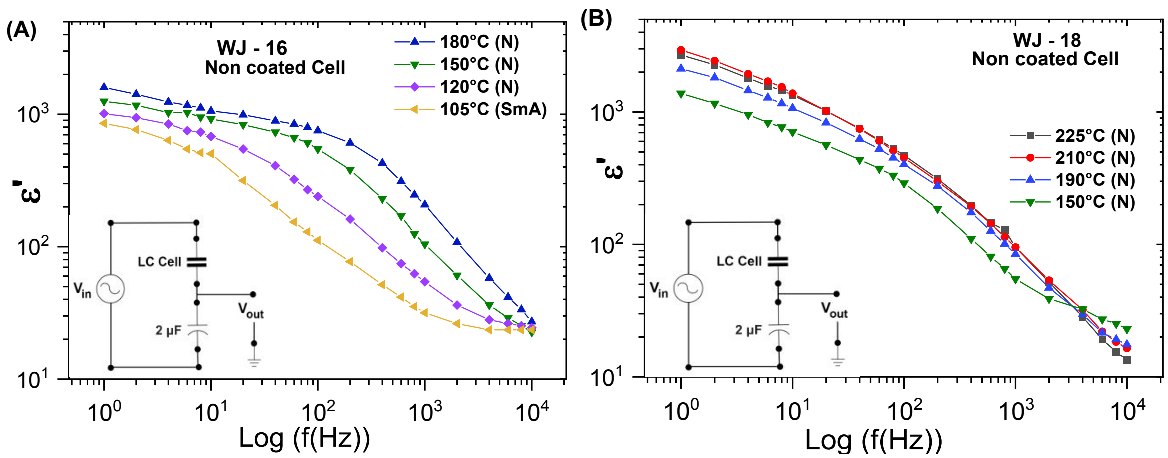

Figure 6. The direct measurement of dielectric permittivity (ε′) as a function of frequency for different temperatures using the capacitance voltage divider circuit using uncoated 4 μm cells filled with (A) WJ-16 and (B) WJ-18. The inset in figure 6B shows a simple capacitance divider circuit used in the measurement of ε′, where V_{in} is applied sin-wave voltage and V_{out} in the output voltage taken from 2 μF capacitor.

It is interesting to note that the frequency dependence of the dielectric permittivity calculated from direct capacitance measurements using uncoated cells of both samples (Figure 7A,B) match with the values measured by dielectric spectroscopy (Figure 5). The result demonstrates CP in both the N and SmA phases.

A direct measurement of the dielectric permittivity provides a clear and direct evidence for the observation of colossal dielectric permittivity of non-ferroelectric compounds, WJ-16 and WJ-18. Hence, this behavior can only be related to superparaelectricity (SPE) [5, 59] in soft matter systems. Superparaelectricity reflects an incomplete ferroelectric long-range order. Ferroelectric state is an assembly of the long-range-ordered polar domains having spontaneous polarization (*Ps*) and it exhibits hysteresis in the polarization as function of the external electric field, while the superparaelectric state consists of the short-range polar order clusters. For the latter, the macroscopic polarization <Ps> ~ 0 and a hysteresis free P–E curve is observed. Figure 7 is a schematic of the proposed dipolar structures in WJ-16 for the three phases. Both states, superparaelectric and the ferroelectric, show large dielectric permittivity.

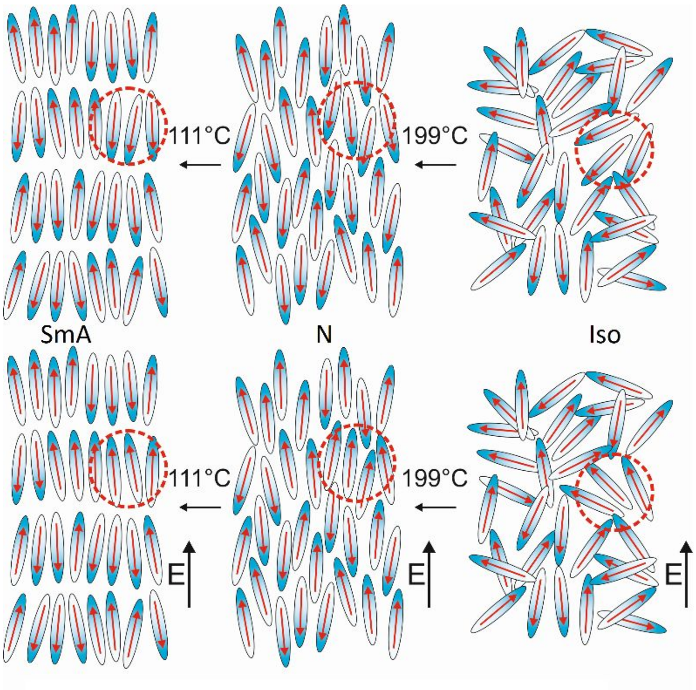

Figure 7. The proposed schematics of dipolar structures and the molecular assembly in the phase sequence of WJ-16.

However, our studied compounds W-16 and WJ-18 exhibit colossal permittivity even in the isotropic phase with the absence of hysteresis in all phases. Therefore, phases of these compounds can be assigned superparaelectrics rather than to ferroelectrics. The higher values of dielectric permittivity can be explained using the classical approach suggested by Kirkwood and Frohlich, [60] where the static dielectric permittivity ϵ_S in paraelectric isotropic liquids is given by:

$$\epsilon_S - n^2 = \frac{3\,\epsilon_S}{2\epsilon_S+n^2}\frac{N}{3\,kT\epsilon_0}\,\mu\mu^* \qquad (2)$$

n is the refractive index at a visible wavelength, kT is the thermal energy, μ is the dipole moment of the molecule, ϵ_0 is the permittivity of free space. μ^* is the average moment of the dipoles in a macroscopic spherical region surrounding the dipole on the assumption that one of the dipoles is kept in a fixed direction. N is the number density of molecules. M/d is the molar volume, N_A is the Avogadro number; $N \cdot \frac{M}{d} = N_A$ and $\mu\mu^* = \mu^2\,(1 + z\overline{\cos\gamma})$, where $\overline{\cos\gamma}$ is the average of the cosine angle between the neighboring molecules, z is the average number of the interacting dipoles, also called the coordination number. Assuming $\overline{\cos\gamma}$ equal to unity, the dielectric permittivity is proportional to the square of the dipole moment and to the coordination number, z plus one. A ferroelectric copolymer with the permittivity of 130 has a coordination number of 30 [61], while the coordination number of 1000 was reported in a bent core compound [54].

In solid state SPE systems, dielectric permittivity is temperature dependent because it depends on the size of ferroelectric domains/clusters but not on the size of the sample. Contrary to this the dielectric strength of a ferroelectric LC is proportional to the thickness of the cell and this observed in different phases such as surface-stabilized SmC* [46], bent-core LCs [54] and ferroelectric nematic N_F [15,16]. This implies that liquid crystals have a long-range directional order, and the correlation length is limited by the cell thickness. Therefore the molecular dynamics can be modeled with boundary condition at the electrodes which gives a linear dependence of dielectric strength on the cell thickness [15,46,54,57]. Preliminary study of our materials shows that the dielectric strength of SPE relaxation process P1 is proportional to the thickness of the cell (*d*) and the high permittivity in our systems can be attributed to the collective fluctuations of a very large number of molecules having the correlation length ~ *d* like the other ferroelectric LCs mentioned above. However, there is big difference in the results obtained from dielectric spectroscopy of FLCs and our materials. The dielectric strength of ferroelectric materials is strongly dependent on bias voltage which suppresses the ferroelectric Goldstone response [13,15,54,57]. Contrary to this, the dielectric strength of our materials is practically independent of the bias voltage up to 35 V using Novocontrol Alpha Analyzer. Although the dielectric permittivity in N_F and in our sample linearly depends on the cell thickness they have different physical origins, the phason mode in N_F and the amplitude mode in SPE. This needs to be studied further.

4. Conclusion

In this study, we have designed, synthesized, and investigated two novel compounds WJ-16 and WJ-18, as modifications of the prototype DIO. The dipole moments determined using DFT are 10.4 and 14.8 D, respectively. Our original objective was the development of new ferroelectric nematic materials. Surprisingly, both materials show linear, non-ferroelectric, hysteresis-free P - E dependence. Recently Mandle [32] showed that the high magnitude of the dipole moment does not guarantee the formation of ferroelectric nematic phases. Madhusudana [29] theoretically showed the importance of the charge distribution along the molecule for the formation of ferroelectric state. Finally, Li *et al* [31] systematically analyzed more than 100 ferrogenic compounds and defined the Pearson's coefficient (or impact) of different parameters on the formation of the ferroelectric nematic phase. The most important parameters are magnitude of the dipole moment (0.26), the molecular length (0.19) and the angle the dipole moment makes with the long molecular axis (0.16). The dipole moment itself the most important parameter, however it alone cannot guarantee the formation of the ferroelectric nematic phase. Both samples being non-ferroelectric show CP measured using dielectric spectrometer as well as using direct capacitance measurements of the LC cell with uncoated electrodes. Hence, the observed phenomenon is best described as superparaelectric rather than ferroelectric. This is the first direct demonstration of superparaelectricity in liquid crystalline organic materials. The results given in this manuscript highlight the anisotropic properties of the large dipole moment soft matter organic molecular system. The synergistic electrical properties are subtle, interesting, and potentially useful.

Acknowledgment

The work in Dublin was funded by the US-Ireland, SFI 21/US/3788. WJ thanks the CSC, China for a PhD scholarship. YT thanks Faculty of Engineering, University of Sheffield for his PhD studentship. MS thanks Prof. Manjuladevi V, BITS Pilani, India for allowing him to work as visiting student at Trinity College Dublin. The work in Sheffield was funded by EPSRC (EP-T003294). GHM thanks Diamond Light Source, UK for beamtime allocations SM31552 and SM33389. XZ thanks Dr. Olga Shebanova and Prof. Nick Terill at station I22, Diamond Light Source for help with SAXS/WAXS experiments.

References

---

[1] L. E. Cross, *Ferroelectrics*, 1987, **76**, 241-267]

[2] T. Park, Z. Nussinov, K. R. A. Hazzard, V.A. Sidorov, A.V. Balatsky, J.L. Sarrao, S.-W. Cheong, M.F. Hundley, Jang-Sik Lee, Q.X. Jia, and J.D. Thompson, *Phys. Rev. Lett.* 2005, **94**, 017002.

[3] X. Q. Liu, S. Y. Wu, X. M. Chen, H. Y. Zhu, *J. Appl. Phys*. 2008, **104**, 054114.

[4] N. N. Rabin, S. Ida, M. R. Karim, Md. S. Islam, R. Ohtani, M. Nakamura, M. Koinuma, L. F. Lindoy, S. Hayami, *ACS Omega* 2018, **3**, 2074−2083.

[5] K. Wang, J. Ouyang, M. Wuttig, Yu-Y. Zhao, H. Cheng, Y. Zhang, R. Su, J. Yan, X. Zhong, F. Zeng, *Adv. Energy Mater*. 2020, **10**, 2001778

[6] R. Waser, *Integrated Ferroelectrics*, 1997, **15**, 39-51.

[7] H. Nishikawa, K. Shiroshita, H. Higuchi, Y. Okumura, Y. Haseba, S. Yamamoto, K. Sago, H. Kikuchi. *Adv. Mater*. 2017, **29**, 1702354

[8] R. J. Mandle, S. J. Cowling, J. W. Goodby, *Phys. Chem. Chem. Phys.* 2017, **19**, 11429-35.

[9] X. Chen, E. Korblova, D. Dong, X. Wei, R. Shao, L. Radzihovsky , M. A Glaser, J. E. Maclennan, D. Bedrov, D. M. Walba, N. A Clark, *Proc. Natl. Acad. Sci. U.S.A*. 2020, **117**, 14021.

[10] R. J. Mandle, S. J. Cowling, J. W. Goodby, *Liq. Cryst*. 2021, **48**, 1780.

[11] N. Sebastian, M. Copic, A. Mertelj, Phys. *Rev. E,* 2022, **106**, 021011.

[12] M. T. Máthé, B. Farkas, L. Péter, Á. Buka, A. Jákli, P. Salamon, *Scientific Reports* 2023, **13**, 6981.

[13] N. Vaupotic et al. Dielectric response of a ferroelectric nematic liquid crystalline phase in thin cells. *Liquid Crystals* 2023, **50**, 584–595.

[14] V. Matko, E. Gorecka, D. Pociecha, J. Matraszek, N. Vaupotič. *Phys. Rev. Research* 2024, **6**, L042017

[15] N. A. Clark, X. Chen, J.E. Maclennan, M.A. Glaser, *Phys. Rev. Research* 2024, **6**, 013195.

[16] A. Erkoreka, J. Martinez-Perdiguero, R. J. Mandle, A. Mertelj, N. Sebastián, *J. Mol. Liquid*s, 2023, 387, 122566.

[17] A. Adaka, M. Rajabi, N. Haputhantrige, S. Sprunt, O. D. Lavrentovich, A. Jakli. *Phys. Rev. Lett*. 2024, **133**, 038101.

[18] P. Kumari, B. Basnet, M. O. Lavrentovich, O. D. Lavrentovich, *Science* 2024, **383**, 1364–1368.

[19] N. Yadav, Y. P. Panarin, W. Jiang, G. H. Mehl, J. K. Vij, *Phys. Chem. Chem. Phys.* 2023, **25**, 9083.

[20] N. Yadav, Y. P. Panarin, J. K. Vij, W. Jiang, G. H. Mehl, *Liq. Cryst*. 2023, **50**, 1375-1382.

[21] B. Basnet, M. Rajabi, H. Wang, P. Kumari, K. Thapa, S. Paul, M. O. Lavrentovich and O. D. Lavrentovich, *Nat. Comms*, 2022, **13**, 3932.

[22] E. Cruickshank, *Chem. Plus. Chem.* 2024, **89**, e202300726.

[23] H. Kikuchi, H. Matsukizono, K. Iwamatsu, S. Endo, S. Anan, Y. Okumuraet, *Adv. Sci*. 2022, **9**, 2202048.

[24] Y. Song, J. Li, R. Xia, H. Xu, X. Zhang, H. Lei, W. Peng, S. Dai, S. Aya, M. Huang. *Phys. Chem. Chem. Phys*. 2022, **24**, 11536.

[25] H. Matsukizono, K. Iwamatsu, S. Endo, Y. Okumura, S. Anan, H. Kikuchi, *J. Mater. Chem. C* 2023, **11**, 6183.

[26] H. Nishikawa, F. Araoka, *Adv. Mater*. 2021, **33**, 2101305.

[27] A. Manabe, M. Bremer, M. Kraska, *Liq. Cryst.* 2021, **48**, 1079.

[28] A. A. Marchenko, O. L. Kapitanchuk, Y. Y. Lopatina, K. G. Nazarenko, A. I. Senenko, N Katsonis, V. G. Nazarenko, O. D. Lavrentovich, *Phys Rev Lett* 2024, **132**, 098101.

[29] N. V. Madhusudana, *Phys Rev. E* 2021, **104**, 014704.

[30] O. E. Panarina, Yu. P. Panarin, F. Antonelli, J. K. Vij, M. Reihmann and G. Galli, *J. Mater. Chem.*, 2006, **16**, 842

[31] J. Li, H. Nishikawa, J. Kougo, J. Zhou, S.Dai, W. Tang, X. Zhao, Y. Hisai, M. Huang, S. Aya, *Sci. Adv*. 2021, 7, eabf5047.

[32] J. Hobbs, C. J. Gibb, and R. J. Mandle, *Small Sci.* 2024, 2400189 .

[33] H. Nishikawa, K. Sano, S. Kurihara, A. Nihoyanagi, G. Watanabe, B. Dhara, F. Araoka *Commun. Mater*. 2022, **3**, 89.

[34] X. Chen, E. Korblova, M. A. Glaser, J. E. Maclennan, D. M. Walba, N. A. Clark, *Proc. Natl. Acad. Sci.* 2021, **118**, e2104092118.

[35] P. Rudquist, *Scientific Reports*, 2021, **11**, 24411.

[36] I. Haller, *Prog. Solid State Chem*., 1975, **10**, 103–118

[37] C. B. Sawyer, C. H. Tower, *Phys. Rev. E*, 1939, **35**, 269.

[38] H. Diamant, K. Drenck, R. Pepinsky, *Rev. Sci. Instrum*. 1957, **28**, 30.

[39] C. Reynaerts, A. de Vos, *Ferroelectrics* 1991, **113**, 439.

[40] Y. P. Panarin, *Mol. Mats*. 1993, **1**, 137 https://doi.org/10.21427/1T6S-FZ03

[41] S. Kimura, S Nishiyama, Y. Ouchi, H. Takezoe, A. Fukuda, *Japanese J. Appl. Phys*. 1987, **26**, L255.

[42] V. M. Vaksman, Y.P. Panarin, *Mol. Mats*. 1992, **1,** 147 DOI: 10.21427/D7FF8R.

[43] C. Filipic, T. Carlson, A. Levstik, B. Zekz, R. Blinc, F. Gouda, S. T. Lagerwall and K. Skarp, *Phys. Rev. A* 1988, **38**, 5833.

[44] A. M. Biradar, S. S. Bawa, and Subhas Chandra, Dielectric relaxation in a high-tilt-angle chiral-nematic–smectic-C* ferroelectric liquid crystal., *Phys.Rev.A*, **45**, 7282 (1992).

[45] F. Gouda, W. Kuczynski, S. T. Lagerwall, M. Matuszczyk, T. Matuszczyk and K. Skarp, Determination of the dielectric biaxiality in a chiral smectic-C phase., *Phys.Rev.A*, **46**, 951 (1992).

[46] Yu. P. Panarin, Yu. P. Kalmykov, S. T. Mac Lughadha, H. Xu and J. K. Vij, Dielectric Response of SSFLC Cells., *Phys.Rev.E*, **50**, 4763-4772 (1994).

[47] M. Fukui, H. Orihara, A. Suzuki, Y. Ishibashi, Y. Yamada, N. Yamamoto, K. Mori, K. Nakamura, Y. Suzuki, I. Kawamura., Dielectric Dispersion in the Antiferroelectric Liquid Crystal MHPOBC., *Jpn.J.Appl.Phys*., **29**, L329 (1990).

[48] Yu. P. Panarin, O. E. Kalinovskaya and J. K. Vij, The investigation of the relaxation processes in AFLCs by broad band dielectric and electro-optic spectroscopy., *Liq.Cryst.,* **25(2),** 241-252 (1998).

[49] K. Hiraoka, A. Taguchi, Y Liq.Cryst.,25(2),241-252u. Ouchi, H. Takezoe, A. Fukuda., *Jpn.J.Appl.Phys*., **29**, L103 (1990).

[50] Yu. P. Panarin, O. E. Kalinovskaya, J. K. Vij and J. W. Goodby., Observation and Investigation of the Ferrielectric Subphase with high qT parameter., *Phys.Rev.E*, **55**, 4345 (1997).

[51] F. Kremer, S. U. Vallerien, R. Zentel, H. Kapitza, *Macromolecules,* 1989, **22**, 4040.

[52] N. Yadav, Y. P. Panarin, J. K. Vij, W. Jiang, G. H. Mehl, *J. Mol. Liq*. 2023, **378**, 121570.

[53] L. Guo, E. Gorecka, D. Pociecha, N. Vaupotič, M. Čepič, R. A. Reddy, K. Gornik, F. Araoka, N. A. Clark, D. M. Walba, K. Ishikawa, H. Takezoe, *Phys. Rev. E* 2011, **84**, 031706.

[54] S. Nakasugi, S. Kang, Tso-Fu. M. Chang, T. Manaka, H. Ishizaki, M. Sone, J. Watanabe, *J. Phys. Chem. B* 2023*,* **127***,* 6585−6595.

---

[55] A. Erkoreka, A. Mertelj, M. Huang, S. Aya, N. Sebastian, and J. Martinez-Perdiguero, *J. Chem. Phys.* 2023, **159**, 184502.

[56] S. Brown, E. Cruickshank, J. M. D. Storey, C. T. Imrie, D. Pociecha, M. Majewska, A. Makal, E. Gorecka, *Chem. Phys. Chem*. 2021, **22**, 2506– 2510.

[57] M. Mrukiewicz, P. Perkowski, J. Karcz and P. Kula, *Phys. Chem. Chem. Phys*., 25,13061 (2023).

[58] M. Mrukiewicz, M. Czerwinski, N. Podoliak, D. Repcek, P. Perkowski, R. J. Mandle and D. Węgłowska, Polar nematic phases with enantiotropic ferro- and antiferroelectric behaviour. *J. Mater. Chem. C* 2024, **12**, 7214–7224.

[59] Ying-Hao Chu, Science Magazine - October 1 (2021).

[60] H. Frohlich, Theory of Dielectrics, Oxford University Press, 1958.

[61] J. G. Kirkwood, *J. Chem. Phys*. 1939, **7**, 911.